Check for updates

Tailored mesoporous γ-WO₃ nanoplates: unraveling their potential for highly sensitive NH₃ detection and efficient photocatalysis†

Shubham Tripathi, [ID] *[a] Jyoti Yadav,[ab] Atul Kumar,[a] Raj Kamal Yadav,[c] Pratima Chauhan,[a] Ravindra Kumar Rawat [ID] [a] and Satyam Tripathi [ID] [ad]

Herein, the monoclinic phase of tungsten oxide (γ-WO₃) was successfully obtained after annealing hydrothermally synthesised WO₃ powder at 500 °C. As per the result obtained from the N_2 adsorption–desorption isotherm, the material has been identified as mesoporous with a specific surface area of 3.71 m^2 g^{-1} from BET (Brunauer–Emmett–Teller) analysis. Moreover, the average pore size (49.52 nm) and volume (0.050 cm^3 g^{-1}) were also determined by the BJH (Barrett–Joyner–Halenda) method. FE-SEM (field emission scanning electron microscopy) and HR-TEM (high resolution transmission electron microscopy) have confirmed the formation of nanoplates with an average diameter of approximately 274 nm. Raman spectroscopy has shown peaks at the lower wavenumber region (270 cm^{-1} and 326 cm^{-1}) and the higher wavenumber region (713 cm^{-1} and 806 cm^{-1}) for O–W–O bending modes and stretching modes, respectively. The combined effect of relative humidity (RH-11%–RH-95%–RH-11%) and NH₃ (150 ppm, 300 ppm, 450 ppm, 600 ppm, 700 ppm, and 800 ppm) was investigated in this reported work. The synthesised γ-WO₃ has shown highly responsive behaviour for humidity of 96.5% (RH-11%–95%) and NH₃ sensing (under humidity) of 97.4% (RH-11%–95% with 800 ppm NH₃). The response and recovery time were calculated as 15 s and 52 s, and 16 s and 54 s for humidity, and NH₃ under humidity, respectively. The experimental findings demonstrated that the resistance of the sensor depends on the concentration of NH₃ and humidity. Moreover, γ-WO₃ has been investigated as a promising catalyst for the dye degradation of methylene blue (MB) with a degradation efficiency of 72.82% and methyl orange (MO) with a degradation efficiency of 53.84% under visible light exposure. This dye degradation occurred within 160 min in the presence of a catalyst under visible light irradiation.

[a] Advance Nanomaterial Research Laboratory, Department of Physics, University of Allahabad, Prayagraj, Uttar Pradesh, 211002, India. E-mail: shubhamtripathi@allduniv.ac.in

[b] Centre of Environmental Science, IIDS, University of Allahabad, Prayagraj, Uttar Pradesh, 211002, India

[c] SGN Government Post Graduate College, Muhammadabad Gohna, Uttar Pradesh, 276403, India

[d] Centre of Material Sciences, IIDS, University of Allahabad, Prayagraj, Uttar Pradesh, 211002, India

† Electronic supplementary information (ESI) available. See DOI: https://doi.org/10.1039/d3cp03353h

Introduction

Tungsten oxides exist in two stoichiometric oxide forms, one being the trioxide form (WO₃), and the other being WO₂. WO₃ is an n-type wide band gap semiconductor with an electronic band gap of ~2.6 eV, and has been extensively researched for a variety of applications.[1] The lowest vacant state of the WO₃ conduction band contains W5d levels. Meanwhile, oxygen (O2p) p-states have the highest energy levels in the valence band. The stoichiometric WO₃ (W^{6+}: $5s^2 5p^6 5d^0$) has an empty 5d conduction band, and hence it functions as an intrinsic semiconductor. Whereas in sub-stoichiometric WO₃ (reduced WO₃, W^{5+}), thermally stimulated donor electrons get partially filled in the 5d conduction band. Consequently, the reduced WO₃ (W^{5+}) behaves as an n-type semiconductor.[2] Numerous different gas-sensitive materials, including metal oxide semiconductors (e.g. Fe₂O₃, ZnO, SnO₂, TiO₂ and WO₃), carbon nanomaterials and conducting polymers with varying performances and sensing methodologies, have been used as gas sensing substances for ammonia sensing over the past few decades.[3–10] Ammonia, a gas broadly used in agriculture production, textile industries, and farming, constitutes one of the most dangerous and flammable environmental pollutants created by mammals or naturally present sources like urea manuring in soils, automobile exhausts, and industrialization.[11,12] Moreover, ammonia is a colourless, hazardous, and flammable gas with a pungent smell. Most people can identify ammonia in the

atmosphere at a lowest level of 5 ppm. The time-weighted typical concentration range for ammonia is 35 ppm for 10 minutes and 25 ppm for 8 hours.[13,14] Furthermore, as the concentration reaches up to 300 ppm, it indicates an immediate risk to life and wellness.[15] Ammonia gas at high concentrations acts as a serious toxic substance, causing harm to the human skin, eyes, and respiratory system.[16] Consequently, for constantly monitoring the leakage of this gas and assurance of health and welfare, the advancement of reliable, long-lasting ammonia gas sensors is considered to be necessary.

Nanostructured metal oxide semiconductors are commonly used in the fabrication of sensors that detect the presence of reducing gases (like NH_3) and oxidising gases (like NO_2). Sensors utilising metal oxide semiconductors have received a significant amount of attention due to their good stability, relatively inexpensiveness, and consistency with microelectronic technology. Because of their structural simplicity, sensitivity and selectivity, an inexpensive and potential survivable metal oxide semiconductor based on WO_3 is of major relevance.[17–19] The WO_3 undergoes an allotropic transformation in response to temperature changes, including polymorphism. WO_3 polymorphs include orthorhombic (β WO_3), tetragonal (α-WO_3), triclinic (δ-WO_3) and monoclinic (γ-WO_3) phases during cooling at temperatures ranging from -180 °C to 900 °C. However, γ-WO_3 is highly stable at room temperature (17 °C to 330 °C).[1] As a typical n-type semiconducting material, WO_3 has distinct physical and chemical characteristics as well as excellent gas sensing properties for a wide range of target gases such as H_2S, NO_2, Cl_2, CO_2, and NH_3. WO_3 is typically used to increase sensitivity at temperatures between 200 °C and 450 °C by speeding up the chemical reactions that take place between the sensing material and the gas.[20] As a result, many real-world applications could benefit from sensors whose working temperature does not surpass 100 °C.[21,22] For the secure monitoring of dangerous gases at room temperature, low-temperature detection methods are preferred.[23] The gas sensing capabilities of metal oxide semiconductors are influenced by the physical and chemical properties of a substrate *via* thick film technology. The rough surface substrate has a substantial impact on its gas sensing capabilities; numerous researchers have shown that substrates with a rough surface are better for gas sensing capabilities.[24]

WO_3 is one of the most promising nanostructured materials for photocatalysis and photo-electrocatalysis because it is a composition of perovskite units. As per previous reported research, about 12% of the solar spectrum is absorbed by it (E_g = 2.5–2.8 eV). Moreover, it has greater electron transport (*ca.* 12 cm^2 V^{-1} s^{-1}) than TiO_2 (0.3 cm^2 V^{-1} s^{-1}) and milder hole diffusion length (*ca.* 150 nm) than α-Fe_2O_3 (2–4 nm). Highly effective photocatalysis, electrochemistry and phototherapy have all benefited from numerous major and positive advancements in materials based on tungsten oxides.[25,26] Herein, the photocatalytic performance was investigated for methylene blue (MB) and methyl orange (MO) as representative dyes. These dyes are chosen as representative dyes because of their widespread consumption and huge pollution in water. In our

findings, γ-WO_3 showed great photocatalytic performance for dye degradation under the exposure of visible light irradiation. Azo dyes do not exist naturally and these are synthetic dyes. Organic substances with the functional group structure R–N═N-R′, in which R and R′ are typically aryl and substituting aryl groups, are referred to as azo dyes. Azo dyes are widely used by the textile industry; however, they are not biodegradable. MB and MO are commonly used dyes. The removal of dyes from wastewater can be accomplished using photocatalytic oxidation technological advances.[27–29] Hence, γ-WO_3 will definitely become a promising material for water purification.

Research and development of innovative methods for sample preparation and synthesis have always played a significant role in the ongoing development of materials research. For a very long time, physicists have been looking for a material synthesis technique that produces high-quality products with minimum production costs and least pollution.[30] In reported work, $Na_2WO_4 \cdot 2H_2O$ has been used without any additional surfactant in order to lower the cost of synthesis. The synthesized γ-WO_3 was characterized by XRD (X-ray diffraction), FE-SEM (field emission scanning electron microscopy), HR-TEM (high resolution transmission electron microscopy), BET (Brunauer–Emmett–Teller), RAMAN spectroscopy and X-ray photoelectron spectroscopy (XPS).

Experimental

Synthesis method, materials used and characterization technique

Sodium tungstate dihydrate ($Na_2WO_4 \cdot 2H_2O$), hydrochloric acid (HCl) and double-distilled water were purchased from Sigma-Aldrich having purity $\geq 99\%$. All chemicals were used without further purification during the synthesis process. 1.5 g of $Na_2WO_4 \cdot 2H_2O$ was dissolved in 100 mL of distilled water and stirred for 1 h using a magnetic stirrer. HCl was added in a drop by drop manner until the pH value of the solution reached 1.5. Then, the prepared solution was transferred into a Teflon-lined autoclave for 24 h at 180 °C. The precipitate was washed several times to remove all impurities and dried at room temperature for 24 h. The obtained precipitate was annealed at 500 °C for 1 h and we get γ-WO_3 (Fig. S1, ESI†). The formation of γ-WO_3 was confirmed by a Rigaku X-ray diffractometer, and the morphology was investigated by FE-SEM (JEOL JSM-7610F) and HR-TEM (TECHNAI G20). For surface area analysis, the BET technique was used while structural analysis was performed by Raman (UniRAM) spectroscopy. For analysing the material's surface chemistry, X-ray photoelectron spectroscopy (XPS) was used.

Fabrication of the sensor and sensing framework

The produced γ-WO_3 material was dissolved in ethanol ($\geq 99.9\%$) and processed together into an evenly mixed slurry. To produce the interdigitated electrode made of fluorine-doped tin oxide (FTO), the formed slurry has been drop cast. We opted to use FTO as an interdigitated electrode as a result of its high

stability, excellent conductivity, and capacity to withstand elevated temperatures. The thick film was heated at 90 °C for 15 minutes in order to eliminate the remaining solvents (moisture and ethanol) from the coated layer. Following that, the γ-WO_3 film was examined at various RH values and NH_3 concentrations. The saturated salt solution was used to create the artificially humid surroundings. The LiCl (RH-11%), $MgCl_2$ (RH-33%), K_2CO_3 (RH-44%), NaCl (RH-75%), and K_2SO_4 (RH-95%) composed this saturated salt solution.[31] The formula shown below was used to determine the NH_3 concentration in parts per million (ppm):[32]

$$1 \text{ ppm} = \frac{RT}{P} \times \frac{1}{M} \times \frac{1 \,\mu\text{g gas}}{1 \text{ L air}}$$

where M, P, T, and R are the molecular weight of the target gas (g mol^{-1}), pressure (Pa), temperature (K), and universal gas constant, respectively. The humidity of the surroundings was monitored using a computerized monitoring system. The electrical resistance variation was examined by a nanovoltmeter (Keithley 2182A) with a current source (Keithley 6221). In our measurement, the voltage and current were kept at 10 V and 2 μA, respectively. The NH_3 gas response (S) was calculated using formula: $S = |\Delta R|/R_{11\%}$.

Photocatalytic activity

The methylene blue (MB) and methyl orange (MO) dyes were used for photocatalytic activity under visible light. The MB and MO were purchased from a local market. The absorption spectra of MB and MO were recorded by an ultraviolet (UV)-visible spectrometer. A halogen lamp (500 Watt) was used as a visible light source. The photocatalytic degradation capability of the hydrothermally synthesized γ-WO_3 nanoparticles was examined *via* degradation of (MB) and (MO) dyes under visible light irradiation. The synthesized γ-WO_3 nanoparticles were used as a catalyst in the photocatalytic degradation experiment. For the photocatalytic experiment, 5 ppm aqueous dye solution was prepared for diluting the 50 ppm stock solution of MB and MO dye. 10 mg of photocatalyst (γ-WO_3) was added to 20 mL of the prepared 5 ppm aqueous dye solution and kept in the dark for 30 min under continuous magnetic stirring, to maintain adsorption–desorption conditions. Moreover, the dye solutions were irradiated using a visible light source. A UV-visible spectrometer was used to measure the degradation of the dye. The irradiated dye solution was collected and centrifuged at every 20 min time interval. The degradation efficiency for the MB and MO dyes was calculated by using the following formula:[33]

$$\text{Degradation efficency } (\eta) = \left(1 - \frac{C_t}{C_0}\right) \times 100 (\%)$$

where C_0 is the absorbance of the dye solution at the initial state of the dye before irradiation and C_t is the absorbance of the dye solution at regular time interval 't' irradiated after the visible light source.

Investigation of functioning species along with the free radical capturing experiment: scavenger analysis

Implementing a scavenger analysis, it was determined whether active species were present during the photocatalytic breakdown of MB adopting γ-WO_3 as a photocatalyst. To determine the presence of superoxide anion radicals $^{\bullet}O_2^{-}$, h^{+} radicals, e^{-} and hydroxyl radicals ($^{\bullet}OH$), the benzoquinone (BQ), ethylenediaminetetraacetic acid (EDTA), $AgNO_3$ and isopropanol (IP) scavengers, respectively, were used in this investigation. The γ-WO_3 photocatalyst was introduced to the MB dye solution together with these scavengers and a degradation investigation was performed.

Results and discussion

X-Ray diffraction analysis

XRD is a non-destructive way of obtaining crystallite size, lattice properties and crystalline phase. The peak position of the XRD pattern of the synthesized γ-WO_3 was well matched with JCPDS no. 83-0950. This reveals the monoclinic crystal structure (γ-WO_3) of the synthesized WO_3 with lattice parameters $a = 7.3$ Å, $b = 7.5$ Å and $c = 7.7$ Å. The XRD peaks were found at (002), (020), (200), (120), (−112), (022), (202), (−122), (−222), (320), (132), (−321), (004), (040), (400), (−114), (024), (204), (240), (420), (−240), (242), (−314), (324), (−512), (404), (116) and (600) (Fig. 1a). Using the Bragg's diffraction condition ($2d \sin\theta = n\lambda$), the inter-planar spacing was also calculated using XRD.
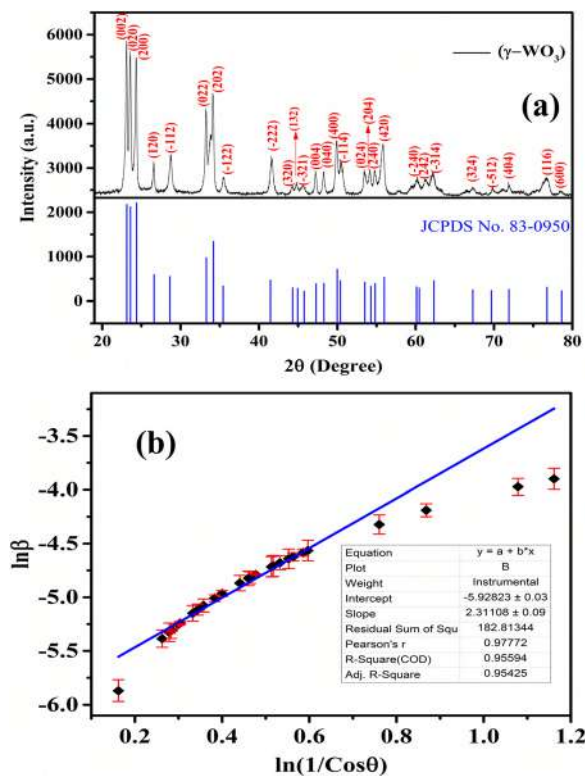

Fig. 1 (a) XRD pattern of the synthesised γ-WO_3; (b) modified Scherrer plot for the synthesised γ-WO_3.

The main peak was observed at 23.19° (2θ) and the inter-planar spacing was calculated as 3.82 Å using a monochromatic X-ray source of wavelength 1.54 Å. Compared to the Scherrer equation, the modified Scherrer equation is much more precise for the estimation of the crystallite size. The Scherrer equation is given as:

$$D = \frac{K\lambda}{\beta \cos\theta} \text{ or } \beta = \frac{K\lambda}{D \cos\theta}$$

where D is the particle size, $\lambda = 1.54$ Å (wavelength of X-ray source), β = FWHM (peak broadening), θ = incident angle and $K = 0.9$ (shape factor). Now, the Scherrer equation can be rewritten by taking the natural logarithm on both sides as:

$$\ln\beta = \ln\left(\frac{1}{\cos\theta}\right) + \ln\left(\frac{k\lambda}{D}\right)$$

This expression (also known as the modified Scherrer equation) represents the equation of the line with $\ln\beta$ as the y-axis, $\ln\left(\frac{1}{\cos\theta}\right)$ as the x-axis (slope $m = 1$) and the intercept at $\ln\left(\frac{k\lambda}{D}\right)$. The graph (Fig. 1b) of the modified Scherrer equation reveals the crystallite size of 52 nm.

Brunauer–Emmett–Teller (BET) analysis

BET analysis is a scientific technique to calculate surface areas and pore size distributions of different solid materials. This methodology depends on the physical adsorption of inert gases, like nitrogen and argon on the solid layer of the material. A single layer of adsorbed gas is formed when the tiny gas molecules are drawn to the surface of the solid material and cause the porous structure to open up. The nitrogen (N_2) adsorption–desorption isotherm plot obtained from heat treatment of γ-WO_3 at 500 °C for 4 h, is shown in Fig. 2a. The average pore size distributions of γ-WO_3 were determined by BJH plot and shown in Fig. 2b. A hysteresis loop profile was observed in γ-WO_3 during the N_2 adsorption–desorption plot at relative pressures ranging from 0.01 to 0.99 which confirms a Type III compositional isotherm.[34] The specific surface area

from BET analysis was calculated as 3.71 m^2 g^{-1}. The average pore size (49.52 nm) and volume (0.050 cm^3 g^{-1}) were determined by the BJH method. A mesoporous substance is a nanoporous substance that has pores having a diameter ranging from 2 to 50 nm. The average pore size of the synthesized γ-WO_3 confirms the formation of a mesoporous material.

FE-SEM and HR-TEM analysis

By using FE-SEM, the microstructure and surface morphology of the synthesised γ-WO_3 were examined. Fig. 3(d and e) shows the FE-SEM micrograph having resolution 100 000× and 5000, respectively. The surface appearance of FE-SEM reveals the formation of nanoplates with a random distribution. The formation of the porous morphology is a consequence of the random arrangement of the particles, which captures gaseous molecules and offers more reactive sites for applications involving gas sensing. The typical thickness of the formed nanoplates ranges from 24 to 40 nm, and the average diameter of the nanoplates was found to be approximately 274 nm. The development of the microstructured nanoplates was subsequently confirmed by the HR-TEM image of γ-WO_3. The average diameter of the particles (214 nm) and the plate thickness observed in the HR-TEM image (Fig. 3(a–c)) are both in good agreement with the information that has been found in the FE-SEM image (Fig. S2, ESI†).

Raman spectroscopy

Raman spectroscopy serves as a non-destructive tool for a chemical investigation that offers adequate information on crystal structure, phase, chemical configuration, polymorphy, and interactions among molecules. It depends on how light interacts via chemical interactions in a substance. The Raman spectrum of the synthesised γ-WO_3 is shown in Fig. 4. Herein, the spectral peak contains two parts of wavenumber regions, one higher wavenumber region (500–1000 cm^{-1}) and another lower wavenumber region (100–500 cm^{-1}). The two peaks (270 cm^{-1} and 326 cm^{-1}) were observed at the lower wavenumber region, which has been assigned for O–W–O bending
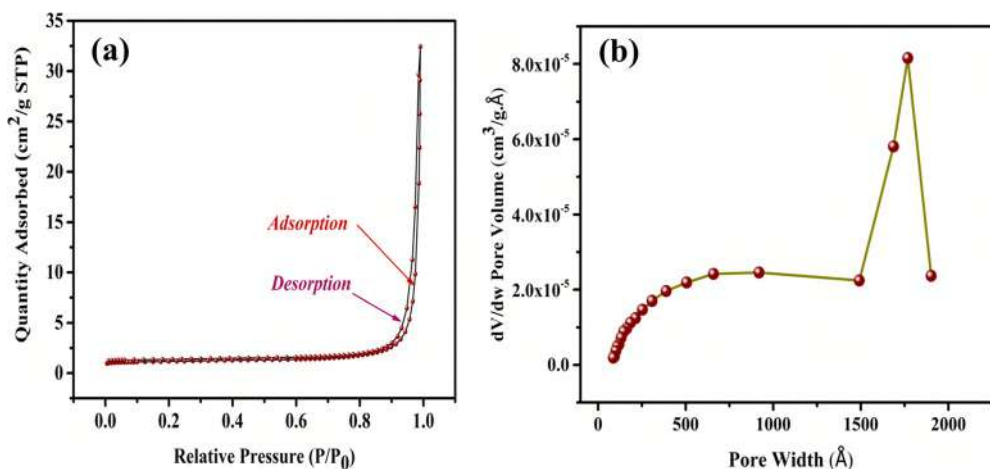

Fig. 2 (a) N$_2$ adsorption–desorption isotherm plot; (b) BJH plot for average pore volume distribution.
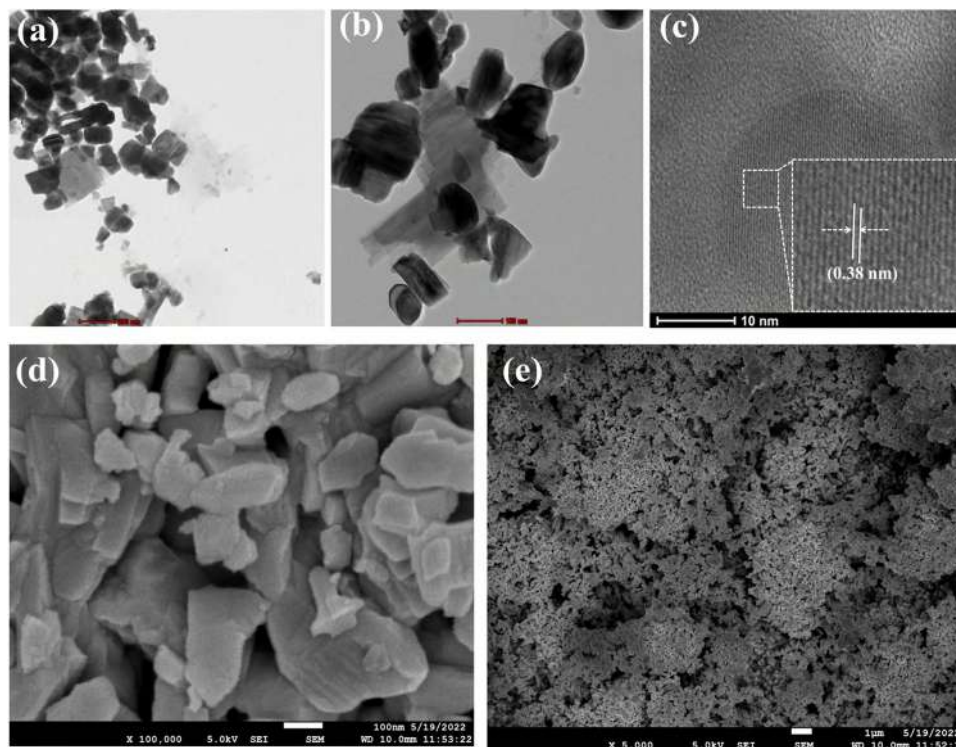
Fig. 3 HR-TEM image of the synthesised γ-WO₃ (a) at 200 nm and (b) at 100 nm, (c) lattice fringes at 10 nm, and FE-SEM image of γ-WO₃ (d) at magnification 100 000× and (e) at magnification 5000×.
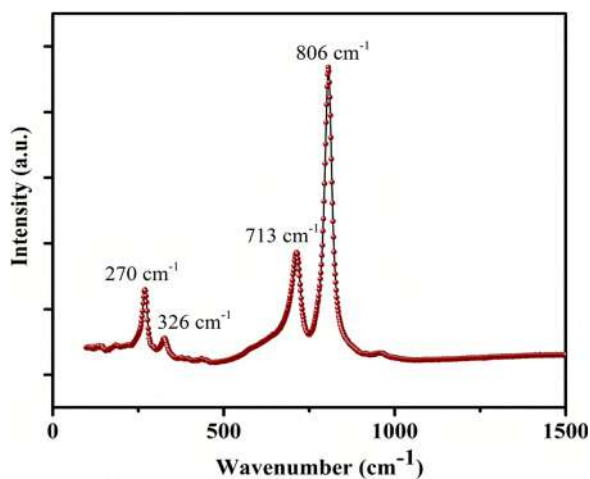

Fig. 4 Raman spectra of the synthesised γ-WO₃.

modes for bridging oxides. Another two peaks (713 cm^{-1} and 806 cm^{-1}) were observed at higher wavenumber region which has been assigned to the stretching mode (Fig. 4). Consequently, these findings confirm the formation of monoclinic WO₃ (γ-WO₃) crystals.[35]

XPS analysis

A material's elemental composition can be determined using the surface-sensitive statistical spectroscopy method known as X-ray photoelectron spectroscopy (XPS), which depends on the photoelectric effect. XPS is an effective technique for identifying not only the elements that are present but also the additional elements to which they are bound. An abundance of tungsten, sodium, oxygen, and carbon has been observed in the XPS spectra of the nanostructured γ-WO₃ films, which are shown in Fig. 5a. W 4f spectra and O 1s spectra are shown in Fig. 5(b and c), respectively. In order to determine the existence of the by-products of the sodium tungstate precursor, the Na 1s peak at 1071 eV was observed. The main peak of the O 1s spectrum was found to be at 530 eV (Fig. 5c). Fig. 5b shows the resolution of the W 4f orbital into W $4f_{5/2}$ and W $4f_{7/2}$ at 37.28 eV and 35.06 eV, respectively. There is no confirmation of the formation of WO_{3-x} because no peak was observed at 34.8 eV as reported by other research groups.[36]

Application of γ-WO₃ as an NH₃ sensor

The electrical resistance-based investigation of the synthesised γ-WO₃ film was carried out over various relative humidity (RH) levels (11–95%) and NH₃ concentrations (150–800 ppm) in order to evaluate the impact of H₂O and NH₃ on the γ-WO₃ nanomaterial at room temperature. Fig. 6a reveals the comparative investigation under 1000 ppm of NH₃, the electrical resistance falling off at every level of RH (11–33–11%, 11–44–11%, 11–54–11%, 11–74–11% and 11–95–11%). The high humidity level (RH-95%) is not useful due to the total saturated state of water molecules on the surface of the γ-WO₃ sensing layer than the low humidity level (Fig. 6a).[37] The corresponding fall off in resistance at different humidity levels indicates that
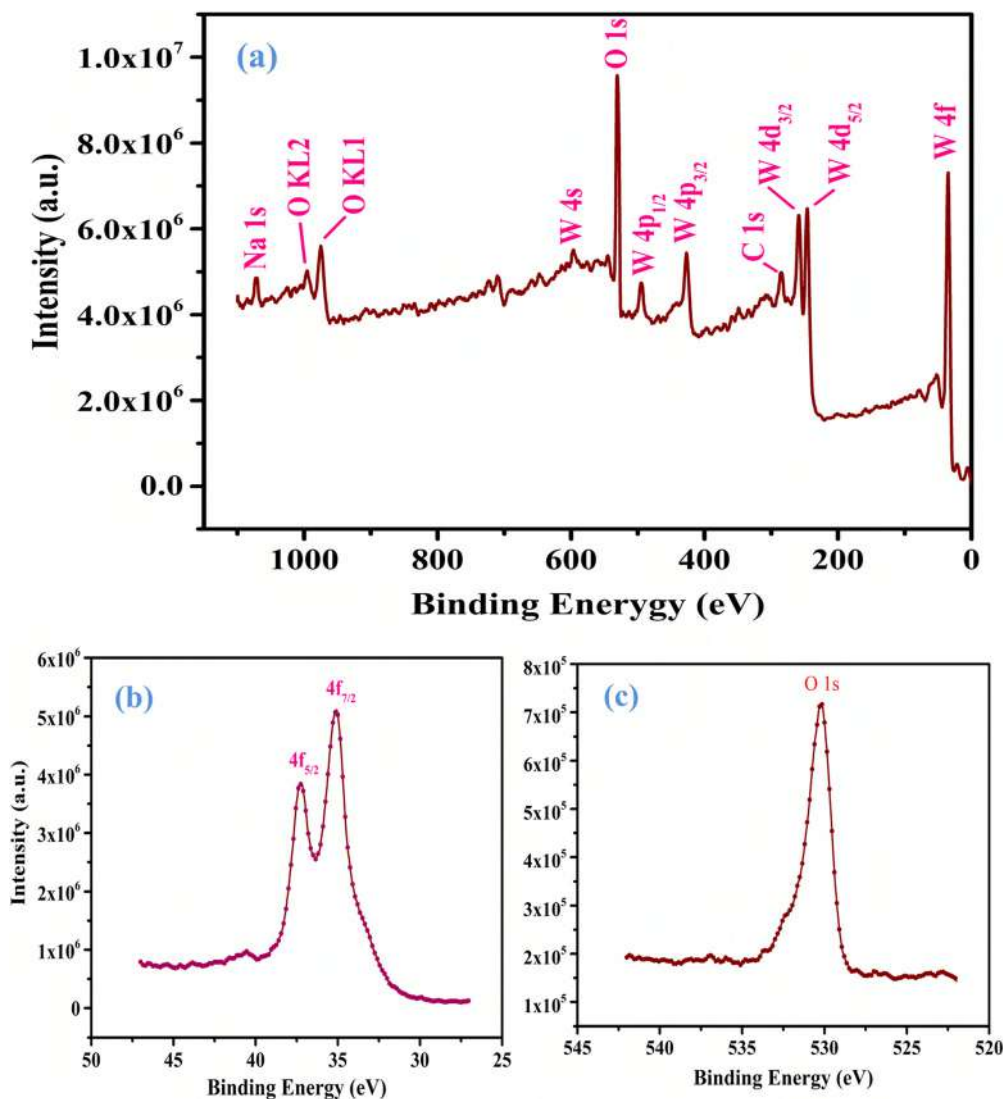
Fig. 5   XPS spectra of the synthesised γ-WO$_3$: (a) XPS survey, (b) W 4f spectrum and (c) spectrum of O1 s.

the H$_2$O and NH$_3$ molecules have strong competition on the γ-WO$_3$ surface. The primary aspects of the humidity sensing framework are the physical and chemical processes involved in adsorption.[38] Under the exposure of γ-WO$_3$ at low RH, the water molecules adhere to the active sites of the γ-WO$_3$ by a chemical adsorption method. In order to form a continuous layer of H$_2$O molecules, the small amount of water molecules that are chemically bonded on the sensing surface is insufficient. Because of this, γ-WO$_3$ sensors produce high resistance at low RH values. Since NH$_3$ gas acts as a channel for proton conduction, proton conduction might be enhanced by adding various NH$_3$ concentrations at lower RH levels.[39]

The physically occurring adsorption of water molecules transforms into a chemical adsorption procedure that occurs in the middle RH region (40–60% RH). The diffusion of protic species and the film's conductivity is facilitated by a continuous layer of physisorbed water over a chemisorbed surface.[40] The bind, hop, and releasing steps are followed by the H$^+$ ions as

they propagate *via* the degenerative system, in accordance with the Grotthuss mechanism (Fig. S4, ESI†). Multiple layers of physisorbed water completely envelop the active areas at high RH levels. Consequently, the resistance of the γ-WO$_3$ layer reflects a propensity to get saturated. Ammonia is strongly soluble in water molecules, due to which the reactions of NH$_4^+$ and OH$^-$ ions produce NH$_4$OH.[39] The concentration-based investigation under the exposure of NH$_3$ to different humidity levels was carried out in Fig. 6b. Fig. 6b reveals that the resistance decreases as the concentration of NH$_3$ increases. In contrast to the chemical structure of water, the NH$_3$ demonstrates a tetrahedral structure with a single proton accepter site as well as triple donor proton sites. This indicates that NH$_3$ gas has an overwhelming propensity to form hydrogen bonds with each of the two proton donor sites and two proton acceptor sites of water molecules. Moreover, the responses received by the γ-WO$_3$ sensor to various RH values and NH$_3$ concentrations are shown in Fig. 6c. The response was observed for RH-33%,
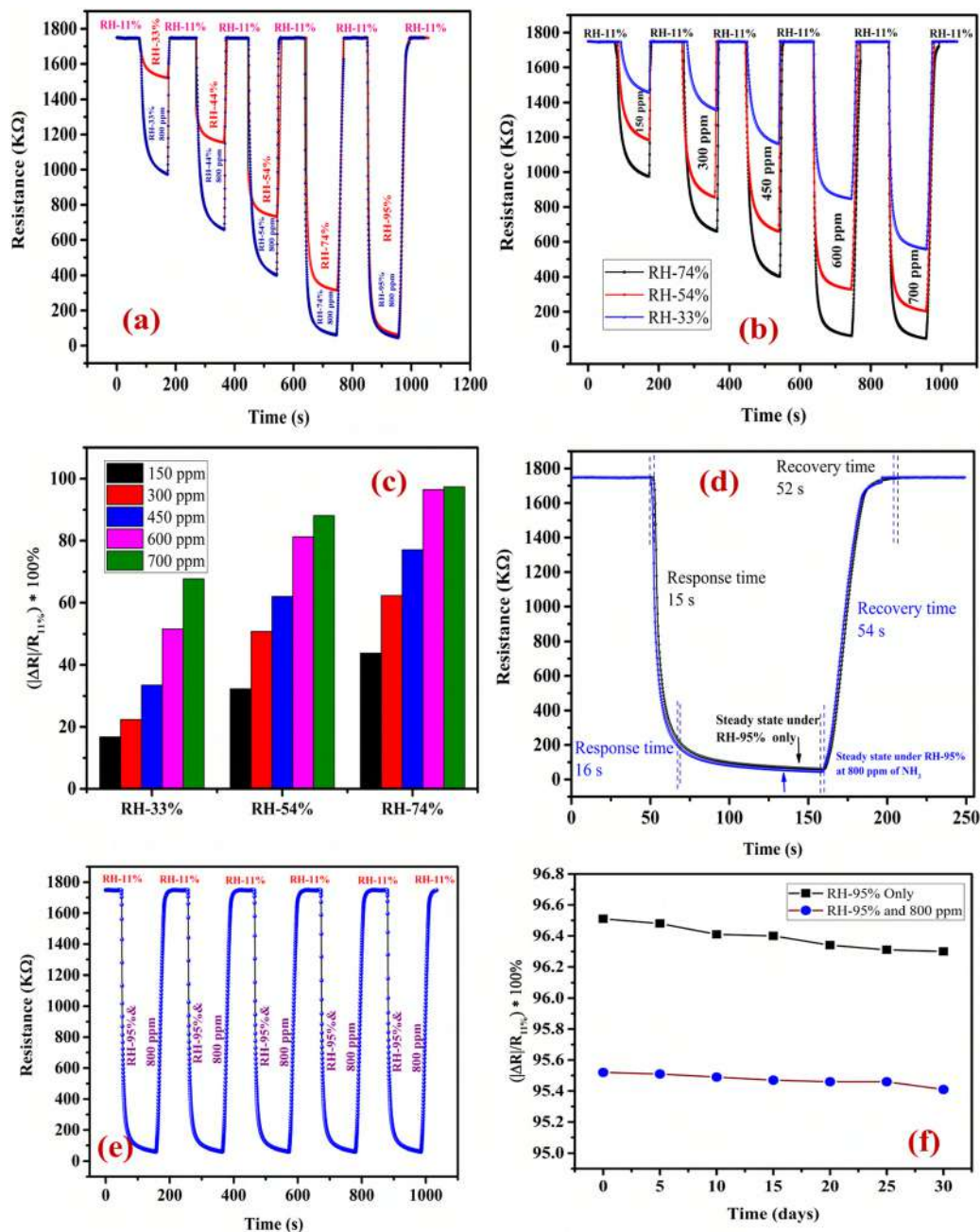
Fig. 6 Electrical resistance-based investigation of γ-WO$_3$. (a) Humidity effect under 800 ppm of NH$_3$; (b) NH$_3$-concentration effect under various RH levels; (c) responses under different exposure conditions; (d) response/recovery time calculation of humidity (RH-11%–RH-95%–RH-11%) and humidity (RH-11%–RH-95%–RH-11%) with 800 ppm of NH$_3$; (e) repeatability of NH$_3$ at 800 ppm under humidity RH-11%–RH-95%–RH–11%; (f) long-term stability investigation for 30 days.

54% and 74% for 150 ppm, 300 ppm, 450 ppm, 600 ppm and 700 ppm. The observed response of the fabricated sensor towards NH$_3$ was found to be interesting, which provides maximum response (97.4%) at RH-95% having concentration 800 ppm. The response observed at RH-75% is almost equal (97.01% at 700 ppm) to the response observed at RH-95% because of saturation. The response and recovery towards RH-11%–RH-95%–RH-11% was calculated as 15 s and 52 s, respectively. Under the exposure of 800 ppm of NH$_3$ with

RH-11%–RH-95%–RH-11%, the response and recovery times were calculated as 16 s and 54 s, respectively (Fig. 6d). The repeatability of the fabricated γ-WO$_3$ sensor was also investigated under RH-11%–RH-95%–RH-11% for 800 ppm. The obtained result is quite interesting because the sensor has shown the best repeatability with very small variation of resistance of 0.893 KΩ to 0.931 KΩ (Fig. 6e). For stability investigation of γ-WO$_3$, the fabricated sensor has been exposed under humidity RH-11%–RH-95%–RH-11% with 800 ppm of NH$_3$ for

Table 1 Comparative study of the γ-WO₃ based sensor with previously reported sensors for humidity and ammonia sensing

Materials	Application	Response	Response/recovery time (s)	Ref.
MXene/CuO	Ammonia sensor	24.8% (RT)	43/26	Wang et al.[41]
RGO/PVP	Humidity sensor	7% (RT)	2.8/3.5	Su et al.[42]
WO₃/Si	Ammonia	10.3% (RT)	17.6/15.4	O. A. Fahad et al.[43]
WO₃/PS	Ammonia	15.2% (RT)	16.2/24.4	O. A. Fahad et al.[43]
$Ti_3C_2T_x$/WO₃-50%	Ammonia	22.3% (RT)	119 s/228 s	X. Guo et al.[44]
rGO/WO₃ nanowire	Ammonia	37^a (at 300 °C)	37 s/711 s	C. M. Hung et al.[45]
WS₂/WO₃ composites	Ammonia	0.38^a (125 °C)	202 s/191 s	Y. Zheng et al.[46]
WO₃ nanoflakes	Ammonia	3.1^a (150 °C)	28 s/68 s	P. S. Kolhe et al.[47]
γ-WO₃	Humidity sensor/humidity sensor under NH₃ exposure	96.5% (RH 11–95%)/97.4% (RH 11–95% with 800 ppm NH₃)	15 s & 52 s/16 s & 54 s	This work

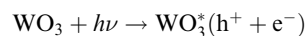^{a} Response = R_{air}/R_{gas}, RT = room temperature.

30 days (Fig. 6f). The sensor response decreased by only 0.22% under RH-95% while the sensor response decreased by 0.12%. Consequently, this result confirms that the γ-WO₃ based sensor has great stability. The comparative study of the synthesized γ-WO₃ with other reported works for ammonia sensing is shown in Table 1.

γ-WO₃ as a photocatalytic application

A visible light source was used to irradiate the photocatalytic degradation experiment. The optical band gap of the γ-WO₃ nanomaterial was calculated from UV-Visible spectroscopy and found as 2.6 eV using the Tauc plot (Fig. S3, ESI†). The absorbance peaks of the MB and MO dyes were found to be 665 nm and 465 nm, respectively,[41] and employed to track how effectively the catalyst (γ-WO₃) nanomaterial degrades the dyes. The photocatalytic degradation of MB and MO dyes is depicted in Fig. 7a and e, respectively. These figures indicate the change in MB and MO dye concentration depending on the duration of irradiation caused by the photocatalyst. Each degradation cycles clear that the concentration of MB and MO dye decreases as the irradiation time passes. Therefore, under the influence of visible light, the synthesized γ-WO₃ can degrade MB and MO dye easily. Fig. 7b and f illustrate the variation of the initial concentration over the final concentration with respect to the duration of time that the dyes (MB and MO) were exposed to radiation. Fig. 7c and g reveal the degradation efficiency of MB and MO, respectively. From plotted graph it has been observed that MB and MO have a degradation efficiency of 72.82% and 53.84%, respectively. This degradation occurred within 160 min in the presence of the photocatalyst under visible light irradiation. These findings unequivocally demonstrate that the hydrothermally synthesized γ-WO₃ nanoparticles have efficient ability to degrade MB and MO dyes. The reusability test was carried out five times in order to investigate the photocatalyst's ability to be reused. The photocatalyst was separated from the dye solution for this test using centrifugation, and it was rinsed off thoroughly with deionized water. The obtained catalyst was extracted, dried on a hot plate, and incorporated into a preliminary dye solution of 5 ppm for analysis. The five successive cycles illustrated in Fig. 7d and h demonstrate the photocatalyst's capacity to be recycled with respect to the associated photocatalysts for MB and MO dye. These findings

show that there are no noteworthy changes in photocatalytic performance towards MB and MO dye. The γ-WO₃ nanoparticles are hence stable and suitable for industrial use. The aforementioned discussion leads to the conclusion that the γ-WO₃ nanoparticles will play a promising role for photocatalytic applications. Moreover, the comparison table of the γ-WO₃ photocatalyst and previously reported photocatalyst is shown in Table 2.

On the basis of the oxidation–reduction reaction that occurs between the dye solution and photogenerated electron–hole pair, the photocatalytic activity of γ-WO₃ nanoparticles may be understood. The dye begins to adsorb on the surface of the photocatalyst when it is added to the dye solution. If this sample is exposed to visible light, there will be an equal number of hole creations in the valence band (VB) as there are excited electrons in the conduction band (CB) of the γ-WO₃ nanoparticles. Superoxide anions (•O₂⁻) and hydroxyl radicals (•OH) are produced when these photogenerated electrons and holes interact with the oxygen and water molecules that were initially absorbed.[52] Moreover, these superoxide anions and hydroxyl radicals react with the dye through oxidation–reduction reaction, and degrade MB & MO dyes.[53] The following equations show the steps involved in the mechanism of photocatalytic activity.

$$WO_3 + h\nu \rightarrow WO_3^*(h^+ + e^-)$$

$$O_2 + e^- \rightarrow \bullet O_2^-$$

$$H_2O + h^+ \rightarrow \bullet OH$$

$$\bullet O_2^- + MB/MO \rightarrow \text{Degradation products}$$

$$\bullet OH + MB/MO \rightarrow \text{Degradation products}$$
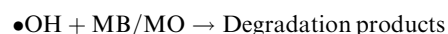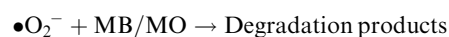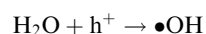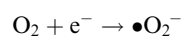
To detect active species (•O₂⁻, e⁻, •OH and h⁺), the BQ, EDTA, AgNO₃ and IP were used as scavengers during the degradation of MB. To understand this mechanism, 1 mmol of scavengers (BQ, EDTA, AgNO₃ and IP) was used for the identification of radicals. It has been confirmed that adding an amount of AgNO₃ had no effect on the efficiency of dye degradation. However, a slight decrement was observed in the presence of EDTA. The effectiveness of IP and BQ's degradation demonstrates that the primary radicals are •OH and •O₂⁻. Consequently, the active species degrade the MB dye in the following
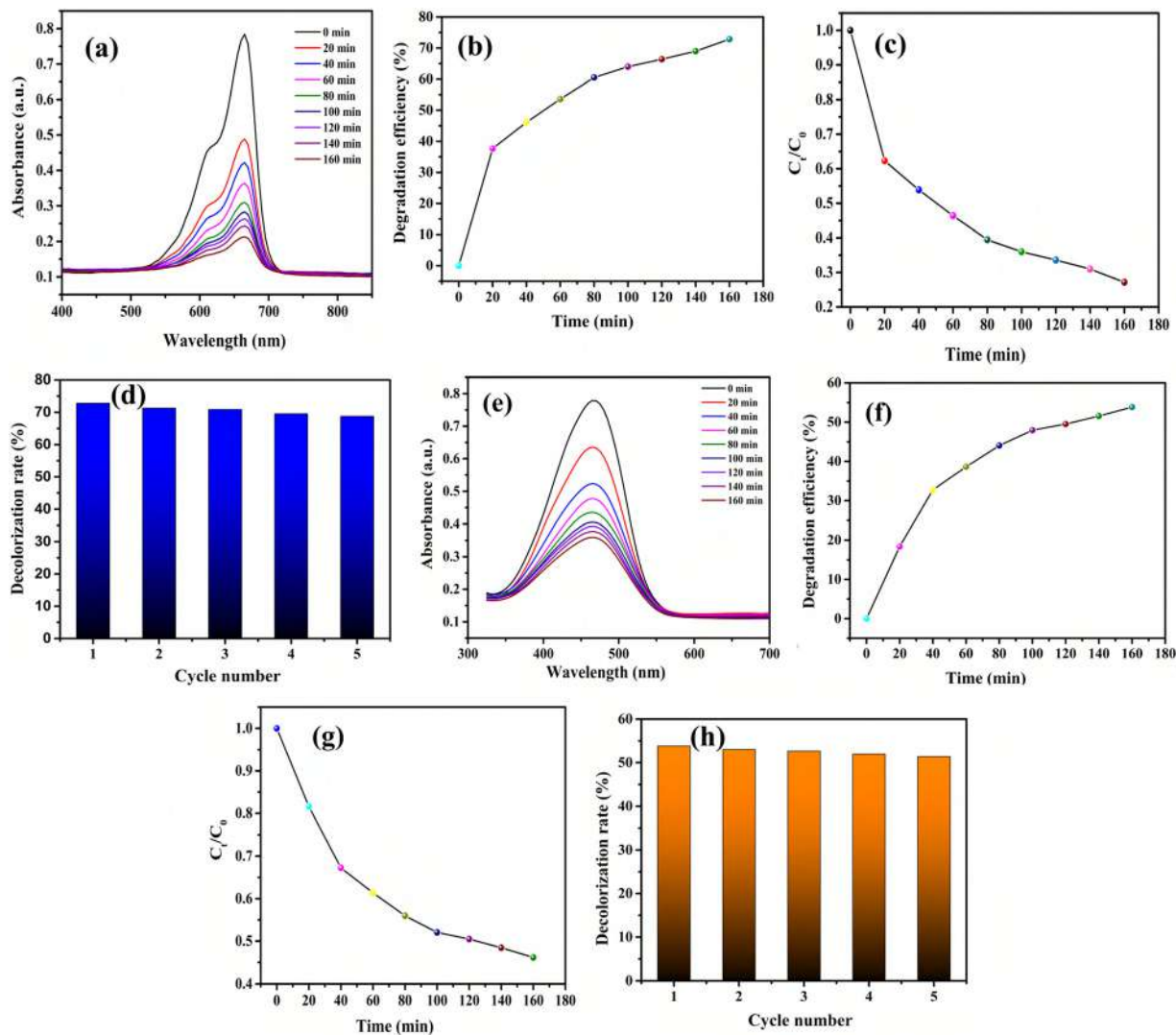
Fig. 7 (a) Photodegradation of MB in the presence of γ-WO$_3$ with respect to time; (b) degradation efficiency plot for MB dye; (c) C_t/C_0 curve of MB dye; (d) reusability test of MB dye; (e) photodegradation of MO in the presence of γ-WO$_3$ with respect to time; (f) degradation efficiency plot for MO dye; (g) C_t/C_0 curve of MO dye; (h) reusability test of MO dye.

Table 2 Comparative study of the γ-WO$_3$ photocatalyst with previously reported photocatalysts

Photocatalyst	Method of synthesis	Photodecomposition	Photocatalytic efficiency (%)	Ref.
rGO–WO$_3$	Thermal decomposition and wet chemistry	MB	65	48
ZnO–graphene	Hydrothermal method	MB	72.1	49
WO$_3$	Acid precipitation method	MB	49	50
Fe$_2$O$_4$	Hydrothermal method	MO	43	51
γ-WO$_3$	Hydrothermal method	MB & MO	72.82 & 53.84	This work

order $^\bullet$O$_2{}^-$ > $^\bullet$OH (Fig. 8c). Moreover, the photocurrent of the electrodes has been determined under light pulses with a duration of 20 s to assess their photoresponse under visible light illumination. The γ-WO$_3$ electrode possessed a stable photocurrent at an applied potential of 0.6 V, demonstrating that the carriers produced by photons in the typical γ-WO$_3$ sample get easily recombined. For repeated on/off cycles, the γ-WO$_3$ electrode's photocurrent response shows good repeatability

(Fig. 8a). The Mott–Schottky graphs of $1/C_{sc}{}^2$ (C_{sc} is space-charge capacitance) as a function of the applied potential are shown in Fig. 8b. The sample showed a positive slope, indicating that γ-WO$_3$ belongs to the n-type semiconductor.[54] In order to determine the flat band potential, the graph was projected to $1/C_{sc}{}^2 = 0$, which resulted in a value of 0.59 volt for the γ-WO$_3$ electrodes (Fig. 8b). A schematic diagram of the photocatalytic and NH$_3$ sensing mechanism is shown in Fig. 9a and b.
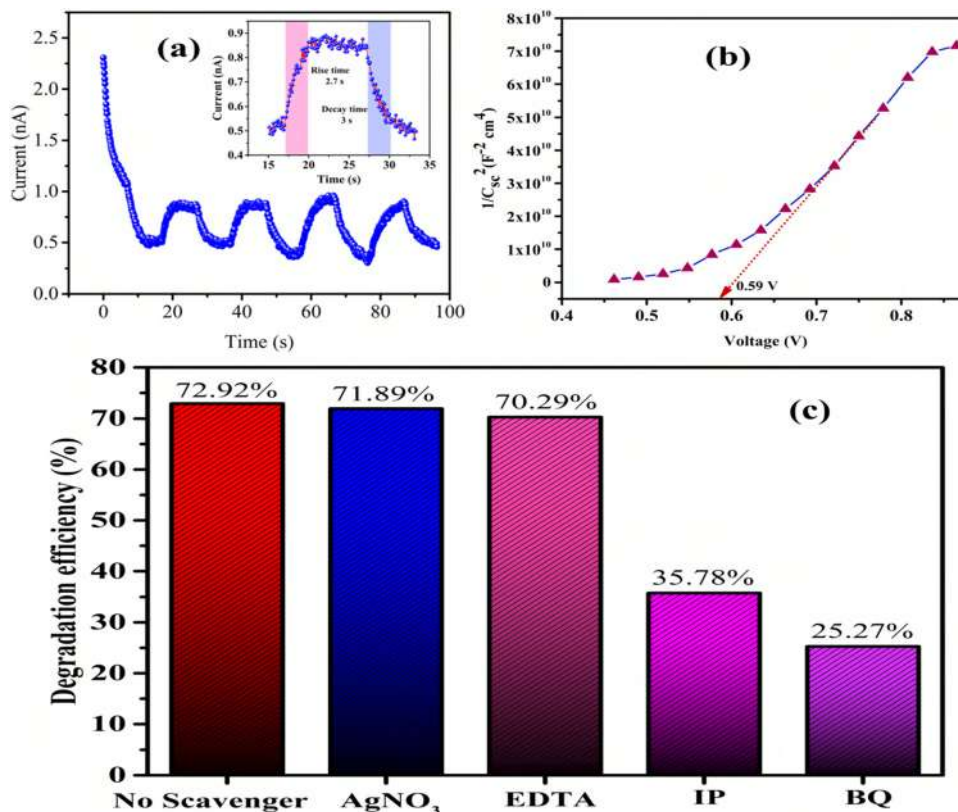
Fig. 8 (a) Photoresponse of γ-WO₃ including rise time and decay time (inset); (b) Mott–Schottky plot; (c) degradation efficiency of MB for the γ-WO₃ photocatalyst under the effect of scavengers (AgNO₃, EDTA, IP, and BQ).
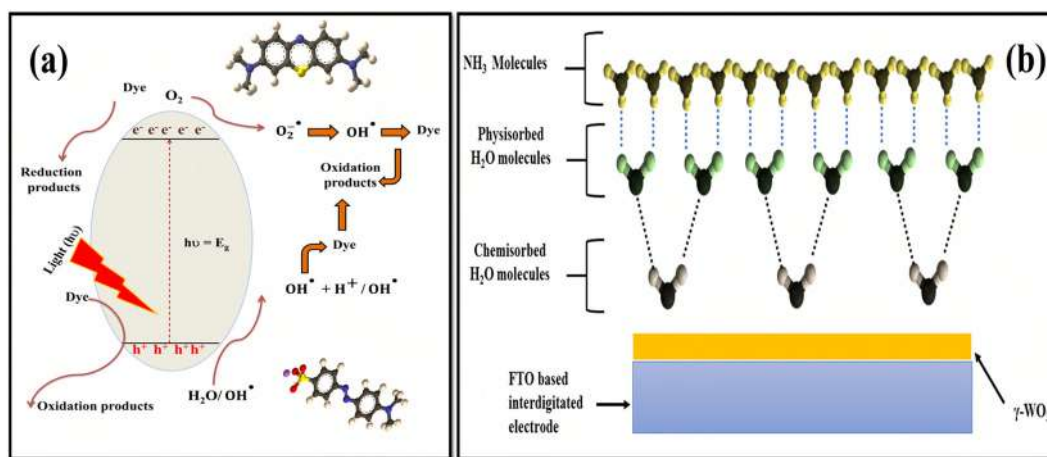

Fig. 9 Schematic diagram for (a) the dye degradation mechanism of MB and MO under visible light irradiation and (b) the NH₃ detection mechanism.

Conclusion

In summary, the XRD technique was used to analyse the synthesised material at room temperature and it was identified as γ-WO₃. The average pore size, pore volume and specific surface area were calculated as 49.52 nm, 0.050 cm³ g⁻¹ and 3.71 m² g⁻¹, respectively from BET analysis. The pore size confirms the formation of mesoporous γ-WO₃. The surface

morphology was investigated by FE-SEM and HR-TEM, clearly confirming the formation of a nanoplate-like structure. The sensing film was deposited on FTO based interdigitated (IDE) electrodes by a spin coater at 2000 rpm. The humidity and ammonia effect was observed in electrical resistance-based analysis of γ-WO₃. The maximum response was investigated for humidity (RH-11%–RH-95%–RH-11%) and ammonia

(800 ppm under RH-95%) as 96.5% and 97.4%, respectively. The fast response and recovery time for humidity (RH-11%–RH-95%–RH-11%) and NH_3 were calculated as 15 s/52 s and 16 s/54 s, respectively. A good sensor repeatability was also observed for the prepared sensor, which confirms the stability of the sensor. Furthermore, the stability was again tested for 30 days observation which shows that the response of the sensor is stable for a long period of time. Moreover, the photocatalytic behaviour was also investigated, which has shown very interesting results for dye degradation. The MB and MO dyes have been degraded using γ-WO_3 as catalyst with 72.82% and 53.84%, respectively. The prepared γ-WO_3 may be a promising agent for sensing as well as catalysis for dye degradation. The findings confirm that our sensor can effectively identify pollutants in our atmosphere as well as for wastewater treatment.

Author contributions

Shubham Tripathi: writing – original draft, data curation, investigation, methodology, Jyoti Yadav: formal analysis, Atul Kumar: validation, Raj Kamal Yadav: resources, visualization, Ravindra Kumar Rawat: conceptualization, Pratima Chauhan: supervision, project administration, Satyam Tripathi: editing final manuscript.

Conflicts of interest

The authors certify that they have no known financial conflicts of interest that would appear to have affected the research presented in this study.

Acknowledgements

References

1 S. Bandi and A. K. Srivastav, *J. Mater. Sci.*, 2021, **56**, 6615–6664, DOI: **10.1007/s10853-020-05757-2**.

2 T. Hirose, *J. Phys. Soc. Jpn.*, 1980, **49**, 562–568, DOI: **10.1143/JPSJ.49.562**.

3 X. Wang, J. Zhang and Z. Zhu, *Appl. Surf. Sci.*, 2006, **252**, 2404–2411, DOI: **10.1016/j.apsusc.2005.04.047**.

4 M. González-Garnica, A. Galdámez-Martínez, F. Malagón, C. Ramos, G. Santana, R. Abolhassani, P. K. Panda, A. Kaushik, Y. K. Mishra, T. V. Karthik and A. Dutt, *Sens. Actuators, B*, 2021, **337**, 129765, DOI: **10.1016/j.snb.2021.129765**.

5 J. Tian, G. Yang, D. Jiang, F. Su and Z. Zhang, *Microchim. Acta*, 2016, **183**, 2871–2878, DOI: **10.1007/s00604-016-1912-6**.

6 J. Li, Y. Lu, Q. Ye, M. Cinke, J. Han and M. Meyyappan, *Nano Lett.*, 2003, **3**, 929–933, DOI: **10.1021/nl034220x**.

7 M. Xue, F. Li, D. Chen, Z. Yang, X. Wang and J. Ji, *Adv. Mater.*, 2016, **28**, 8265–8270, DOI: **10.1002/adma.201602302**.

8 N. Peng, Q. Zhang, C. L. Chow, O. K. Tan and N. Marzari, *Nano Lett.*, 2009, **9**, 1626–1630, DOI: **10.1021/nl803930w**.

9 T. Y. Chen, H. I. Chen, Y. J. Liu, C. C. Huang, C. S. Hsu, C. F. Chang and W. C. Liu, *IEEE Trans. Electron Devices*, 2011, **58**, 1541–1547, DOI: **10.1109/TED.2011.2115245**.

10 A. T. Güntner, M. Righettoni and S. E. Pratsinis, *Sens. Actuators, B*, 2016, **223**, 266–273, DOI: **10.1016/j.snb.2015.09.094**.

11 B. Fungo, J. Lehmann, K. Kalbitz, M. Thiongo, M. Tenywa, I. Okeyo and H. Neufeldt, *Biol. Fertil. Soils*, 2019, **55**, 135–148, DOI: **10.1007/s00374-018-01338-3**.

12 J. Yang, H. Muroyama, T. Matsui and K. Eguchi, *J. Power Sources*, 2014, **245**, 277–282, DOI: **10.1016/j.jpowsour.2013.06.143**.

13 R. K. Gangopadhyay and S. K. Das, *Process Saf. Prog.*, 2008, **27**, 15–20, DOI: **10.1002/prs.10208**.

14 M. J. Fedoruk, R. Bronstein and B. D. Kerger, *J. Expo. Anal. Environ. Epidemiol.*, 2005, **15**, 534–544, DOI: **10.1038/sj.jea.7500431**.

15 V. B. Raj, A. T. Nimal, Y. Parmar, M. U. Sharma, K. Sreenivas and V. Gupta, *Sens. Actuators*, 2010, **147**, 517–524, DOI: **10.1016/j.snb.2010.03.079**.

16 N. Dac Dien, D. Duc Vuong and N. Duc Chien, *Adv. Nat. Sci.: Nanosci. Nanotechnol.*, 2015, **6**, 035006, DOI: **10.1088/2043-6262/6/3/035006**.

17 B. Urasinska-Wojcik, T. A. Vincent and J. W. Gardner, *Procedia Eng.*, 2016, **168**, 255–258, DOI: **10.1016/j.proeng.2016.11.181**.

18 H. Mhamdi, R. B. Zaghouani, T. Fiorido, J. L. Lazzari, M. Bendahan and W. Dimassi, *J. Mater. Sci.: Mater. Electron.*, 2020, **31**, 7862–7870, DOI: **10.1007/s10854-020-03324-8**.

19 W. C. Shen, P. J. Shih, Y. C. Tsai, C. C. Hsu and C. L. Dai, *Micromachines*, 2020, **11**, 1, DOI: **10.3390/mi11010092**.

20 X. Z. Guo, Y. F. Kang, T. L. Yang and S. R. Wang, *Trans. Nonferrous Met. Soc. China*, 2012, **22**, 380–385, DOI: **10.1016/S1003-6326(11)61187-4**.

21 L. Huang, Z. Wang, X. Zhu and L. Chi, *Nanoscale Horiz.*, 2016, **5**, 383–393, DOI: **10.1039/c6nh00040a**.

22 V. Kruefu, A. Wisitsoraat, A. Tuantranont and S. Phanichphant, *Sens. Actuators, B*, 2015, **215**, 630–636, DOI: **10.1016/j.snb.2015.03.037**.

23 S. Tripathi, D. Tripathi, R. K. Rawat and P. Chauhan, *Mater. Lett.*, 2023, **335**, 133840, DOI: **10.1016/j.matlet.2023.133840**.

24 M. Zhang, T. Ning, P. Sun, Y. Yan, D. Zhang and Z. Li, *Ceram. Int.*, 2018, **44**, 3000–3004, DOI: **10.1016/j.ceramint.2017.11.054**.

25 W. Li, P. Da, Y. Zhang, Y. Wang, X. Lin, X. Gong and G. Zheng, *ACS Nano*, 2014, **8**, 11770, DOI: **10.1021/nn5053684**.

26 Q. Mi, A. Zhanaidarova, B. S. Brunschwig, H. B. Gray and N. S. Lewis, *Energy Environ. Sci.*, 2012, **5**, 5694, DOI: **10.1039/C2EE02929D**.

27 L. L. Zhang, J. Du, T. Ran, H. J. Gao and Y. W. Liao, *J. Mater. Sci.*, 2016, **51**, 7186–7198, DOI: **10.1007/s10853-016-9999-z**.

28 Z. J. Zhang, W. Z. Wang and E. P. Gao, *J. Mater. Sci.*, 2014, **49**, 7325–7332, DOI: **10.1007/s10853-014-8445-3**.

29 Z. J. Zhang, T. T. Zheng, J. Y. Xu and H. B. Zeng, *J. Mater. Sci.*, 2016, **51**, 3846–3853, DOI: **10.1007/s10853-014-8445-3**.

30 W. D. Callister, UK, 2000; Volume 471660817.

31 S. Tripathi, D. Tripathi and P. Chauhan, *Journal of Solid State ECS*, 2023, **12**, 3, DOI: **10.1149/2162-8777/acbf75**.

32 E. R. Cohen and B. N. Taylor, *J. Res. Nat. Bur. Stand.*, 1987, **92**, 85, DOI: **10.6028/jres.092.010**.

33 D. Eeksha, P. Kour, I. Ahmed, K. K. Haldar, C. S. Yadav, S. K. Sharma and K. Yadav, *J. Alloys Compd.*, 2023, **960**, 171073, DOI: **10.1016/j.jallcom.2023.171073**.

34 S. Brunauer, L. S. Deming, W. E. Deming and E. Teller, *J. Am. Chem. Soc.*, 1940, **62**, 1723.

35 R. Senthilkumar, G. Ravi, C. Sekar, M. Navaneethan and Y. Hayakawa, *J. Mater. Sci.: Mater. Electron.*, 2015, **26**, 1389–1394, DOI: **10.1007/s10854-014-2552-4**.

36 A. P. Shpak, A. M. Korduban, M. M. Medvedskij and V. O. Kandyba, *J. Electron Spectrosc. Relat. Phenom.*, 2007, **156**, 172–175, DOI: **10.1016/j.elspec.2006.12.059**.

37 B. Soman, S. Challagulla, S. Payra, S. Dinda and S. Roy, *Res. Chem. Intermed.*, 2018, **44**, 2261, DOI: **10.1007/s11164-017-3227-6**.

38 A. Linsebigler, G. Lu and J. T. Yates, *Chem. Rev.*, 1995, **95**, 735, DOI: **10.1021/cr00035a013**.

39 N. Agmon, *Chem. Phys. Lett.*, 1995, **244**, 456, DOI: **10.1016/0009-2614(95)00905-J**.

40 A. Linsebigler, G. Lu and J. T. Yates, *Chem. Rev.*, 1995, **95**, 735, DOI: **10.1021/cr00035a013**.

41 D. Wang, D. Zhang, Y. Yang, Q. Mi, J. Zhang and L. Yu, *ACS Nano*, 2021, **15**, 2911, DOI: **10.1021/acsnano.0c09015**.

42 Y. Su, G. Xie, S. Wang, H. Tai, Q. Zhang, H. Du, H. Zhang, X. Du and Y. Jiang, *Sens. Actuators, B*, 2017, **251**, 144, DOI: **10.1016/j.snb.2017.04.039**.

43 O. A. Fahad and A. S. Mohammed, *Mater. Today: Proc.*, 2021, **42**, 2405–2409, DOI: **10.1016/j.matpr.2020.12.547**.

44 X. Guo, Y. Ding, D. Kuang, Z. Wu, X. Sun, B. Du, C. Liang, Y. Wu, W. Qu, L. Xiong and Y. He, *J. Colloid Interface Sci.*, 2021, **595**, 6–14, DOI: **10.1016/j.jcis.2021.03.115**.

45 C. M. Hung, D. Q. Dat, N. V. Duy, V. V. Quang, N. V. Toan, N. V. Hieu and N. D. Hoa, *Mater. Res. Bull.*, 2020, **125**, 110810, DOI: **10.1016/j.materresbull.2020.110810**.

46 Y. Zheng, L. Sun, W. Liu, C. Wang, Z. Dai and F. Ma, *J. Mater. Chem. C*, 2020, **8**, 4206–4214, DOI: **10.1039/C9TC06686A**.

47 P. S. Kolhe, P. Mutadak, N. Maiti and K. M. Sonawane, *Sens. Actuators, A*, 2020, **304**, 111877, DOI: **10.1016/j.sna.2020.111877**.

48 S. Prabhu, S. Manikumar, L. Cindrella and O. J. Kwon, *Mater. Sci. Semicond. Process.*, 2018, **74**, 136–146.

49 H. Fan, X. Zhao, J. Yang, X. Shan, L. Yang, Y. Zhang and X. M. Li, *Catal. Commun.*, 2012, **29**, 29–34.

50 V. T. Nguyen, H. S. Nguyen, V. T. Pham, T. T. Mai Nguyen, T. L. Anhluu, H. L. Nguyen, D. C. Nguyen and C. T. Nguyen, *Commun. Phys.*, 2020, **30**, 319–330.

51 A. Rshad, J. Iqbal, I. Ahmad and M. Israr, *Ceram. Int.*, 2018, **44**, 2643–2648.

52 A. Roy, S. Arbuj, Y. Waghadkar, M. Shinde, G. Umarji, S. Rane, K. Patil, S. Gosavi and R. Chauhan, *J. Solid State Electrochem.*, 2016, **21**, 9, DOI: **10.1007/s10008-016-3328-y**.

53 R. Saravanan, V. K. Gupta and V. Narayanan, *J. Mol. Liq.*, 2013, **181**, 133, DOI: **10.1016/j.molliq.2013.02.023**.

54 L. Li, X. Zhao, D. Pan and G. Li, *Chin. J. Catal.*, 2017, **38**, 2132–2140.